npj | climate and atmospheric science

Article

Published in partnership with CECCR at King Abdulaziz University

https://doi.org/10.1038/s41612-026-01340-9

A synoptic view of the atmospheric circulation response to SST anomalies in the Kuroshio-Oyashio Extension Region: the importance of latent heating structure

Dong Wan Kim[1] ✉, Young-Oh Kwon[1], Claude Frankignoul[1,2], Clara Deser[3], Gokhan Danabasoglu[3], Adam Herrington[3] & Sunyong Kim[1,4]

The complex nature of extratropical air-sea coupling has hampered a detailed physical understanding of how the atmosphere responds to sea surface temperature (SST) anomalies over the Kuroshio-Oyashio Extension (KOE) region. Departing from the conventional approach of examining the seasonal-mean response, this study focuses on how atmospheric latent heating structures in early winter are modulated by synoptic weather patterns, and how those weather patterns selectively respond to KOE SST anomalies. The results are based on high-resolution atmospheric model experiments (1/8 degree over the North Pacific, tapering to 1 degree over the rest of the globe). While three dominant synoptic weather patterns that enhance latent heating over the KOE region are identified, only one of them, corresponding to anticyclonic baroclinic wave, systematically responds to the imposed SST anomalies. Warm SST anomalies induce stronger updrafts, which enhance atmospheric latent heating and ultimately strengthen and anchor the anomalous anticyclone over the North Pacific. Because this anticyclonic baroclinic system occurs more frequently than other types of weather patterns and has the greatest sensitivity to KOE SST anomalies, it dominates the seasonal-mean atmospheric response. The results demonstrate that a synoptic view is needed for an improved understanding of the mechanisms governing the seasonal-mean atmospheric circulation response to KOE SST forcing.

Western boundary current (WBC) regions such as the Kuroshio-Oyashio Extension (KOE) and Gulf Stream are characterized by strong variability in both the ocean and atmosphere from synoptic to climate time scales[1–3]. While there is an empirical evidence that the atmosphere significantly responds to the KOE variability in the cold season as many studies have probed the mechanisms of WBC air-sea interaction and associated regional and downstream impacts[4–8], a complete understanding is lacking due in part to the pronounced nonlinearity of the seasonal-mean atmospheric response to WBC sea surface temperature (SST) anomalies. Although linear theory predicts a baroclinic downstream low-level cyclonic response to positive SST anomalies[4], studies have shown that the response may differ substantially from linear theory for a variety of reasons, including nonlinear dynamics[5,9,10], background seasonality[11–13], and model resolution[14–17]. One possible source of such lack of consensus on why the response often deviates from linear theory could be associated with the representation of latent heating within a synoptic system – a conduit for SST anomalies to impact the atmosphere[18,19]. While linear theory may explain the direct atmospheric response to latent heating[4], the mechanisms generating a latent heating anomaly, such as convection and moist processes, are inherently nonlinear[20]. Therefore, understanding the characteristics of latent heating structures over WBC regions and how their variability is impacted by underlying SST anomalies associated with oceanic frontal variability may help disentangle the complexity of air-sea coupling mechanisms over the WBC regions and provide a necessary step toward closing the gap between the aforementioned different perspectives.

One important characteristic of latent heating in the extratropics is that it is often associated with a synoptic system[18,20]. While studies have investigated the role of transient storm activity to understand the seasonal mean

[1]Woods Hole Oceanographic Institution, Woods Hole, MA, USA. [2]LOCEAN, Sorbonne université /IRD/CNRS/MNHN, Paris, France. [3]National Science Foundation National Center for Atmospheric Research, Boulder, CO, USA. [4]Current affiliation: APEC Climate Center, Busan, South Korea. ✉e-mail: dong-wan.kim@whoi.edu

climate response to the WBC forcing[21–23], how various types of synoptic weather patterns in which latent heating occurs would selectively respond to oceanic frontal variability is not well understood. Therefore, it motivates us to, first, explore how latent heating anomalies are governed by synoptic circulation patterns in the WBC region and, second, how those synoptic systems respond to a warm SST anomaly. We hypothesize that different meteorological conditions can lead to a strong enhancement of selective latent heating structures, and that the interactions between SST and latent heating anomalies may also depend on the surrounding synoptic conditions. Diagnosing various synoptic weather patterns prior to investigating the seasonal mean signal, and identifying a distinct response of each of those synoptic systems to the SST forcing, may help better categorize dynamically relevant information and prevent canceling out of meaningful signals by considering their time-mean effect.

Recent studies have reported that the simulated atmospheric response to extratropical SST anomalies is sensitive to model resolution since models with finer horizontal resolution can better resolve vertical motions induced by the SST forcings, and hence latent heating[14,17,18]. For example, Smirnov et al.[14] compared the atmospheric responses to a KOE SST anomaly between atmospheric general circulation models (AGCMs) with 1° and 0.25° horizontal resolution and found that the simulated diabatic heating response is balanced by vertical advection at high resolution and by horizontal advection at low resolution. Wills et al.[17] compared the atmospheric response to SST anomalies in the Gulf Stream region in models with 1°, 0.25° and 0.125° resolution and found that the finer the resolution, the more robust and realistic the atmospheric response is. In addition to atmospheric resolution, improving the resolution of prescribed oceanic boundary conditions may also strongly impact the atmospheric response since the resolved mesoscale oceanic eddies can induce stronger localized convective responses than those can be found in coarse resolution models[15,16,24,25].

Inspired by these findings, we conduct high-resolution model simulations to examine how KOE frontal variability in early winter (Nov-Jan) influences different types of latent heating associated with various synoptic weather systems, employing the state-of-the-art Variable Resolution Community Atmosphere Model version 6 (VR-CAM6). The model uses a spectral element dynamical core with an unstructured global mesh grid system[26]. Such a configuration allows us to simulate a target region at high resolution (~1/8°) while maintaining rest of the globe at low-resolution (~1°), thereby keeping the computational costs relatively affordable. This grid system has successfully simulated climate over various regions, including Asia, North America, Arctic, the North Atlantic, and the Mediterranean[17,27–30]. Although Wills et al. showed an improved North Atlantic atmospheric response to the Gulf Stream forcing under enhanced variable resolution grid (~1/8°)[17], such a high-resolution air-sea interaction simulation has not been performed over the North Pacific. Therefore, we expand the application areas of VR-CAM6 by simulating for the first time the North Pacific climate system with enhanced (~1/8°) resolution (Fig. 1). Furthermore, in contrast with previous high-resolution modeling studies of WBC air-sea interactions which used low-resolution boundary conditions[14,17], we have incorporated higher resolution (1/12°) oceanic boundary conditions obtained from the GLORYS12 reanalysis[31]. Combining high-resolution boundary conditions and a high-resolution atmospheric model enables us to represent small-scale features such as oceanic mesoscale eddies, atmospheric frontal-scale updrafts and convective motions that are important for understanding latent heat release within the air-sea coupled system. We first investigate the latent heating structures in a control (climatological SST) experiment (hereafter, CTRL), and then compare their key characteristics in a perturbation experiment by adding an SST anomaly pattern in the KOE region (hereafter, WARM; Fig. 2). Both CTRL and WARM ensemble sets have 43 members, with each different member starting from different initial conditions. Each simulation is integrated from November to January (NDJ). Thus, the analysis is based on 43 early winters when the SST front is neutral (CTRL) and another 43 seasons with the northward shift of the SST front (WARM). Further details of the experimental design are given in the "Methods".

Results

Latent heating characteristics and indices

Our hypothesis is that different types of latent heating structures are associated with various types of weather patterns and that each of them behaves differently in response to the SST anomaly forcing. To test this idea, we first define two different latent heating structures: (1) Large-scale condensational heating, which represents latent heating due to cloud macrophysics and microphysics and is closely associated with processes that are explicitly resolved in the AGCM[32] such as moisture convergence by the large-scale circulation; and (2) Convective heating, which represents latent heating associated with shallow and deep convection and boundary layer mixing, which are parametrized in the AGCM. Although convective heating is closely linked to deep convection over the tropics (ZMDT term[33] of Table 1), over the mid-latitudes shallow convection and mixing account for most of the convective heating (not shown). Such a differentiation is analogous to decomposing precipitation into large-scale precipitation and convective precipitation. Note that this categorization is somewhat dependent on what are the resolved and parametrized processes in the model of choice. Specific variables and equations that define two heating terms are shown in Table 1.

Figure 3 shows the overall characteristics of the two types of latent heating in the model. The NDJ climatology of vertically averaged large-scale condensational heating shows enhanced heating over the mid-latitude storm track regions (Fig. 3a), while convective heating peaks over the intertropical convergence zone and also displays local maxima over the KOE region (Fig. 3b). Pronounced large-scale heating is located throughout the North Pacific basin, but strong extratropical convective heating is

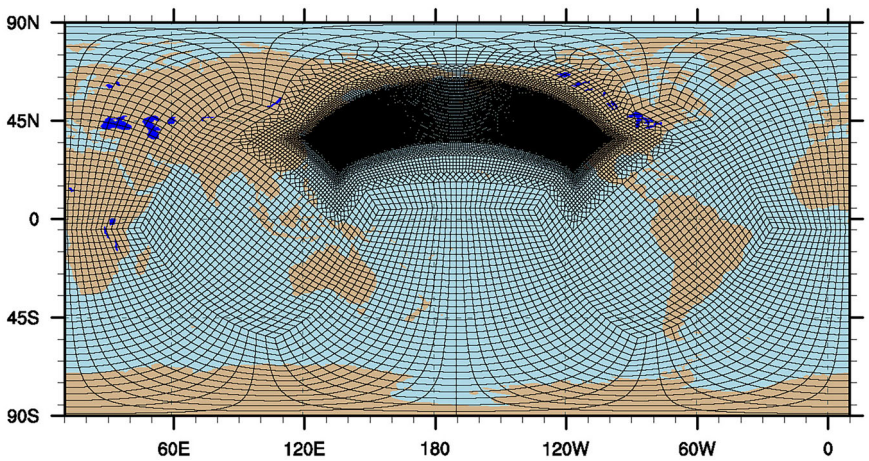

Fig. 1 | The unstructured mesh grid system is used for the Variable Resolution CAM6 simulations. The finest grid resolution over the North Pacific region is ~1/8°, tapering to ~1/2° in the surrounding transition zone; the remainder of the globe has a grid resolution of ~1°.

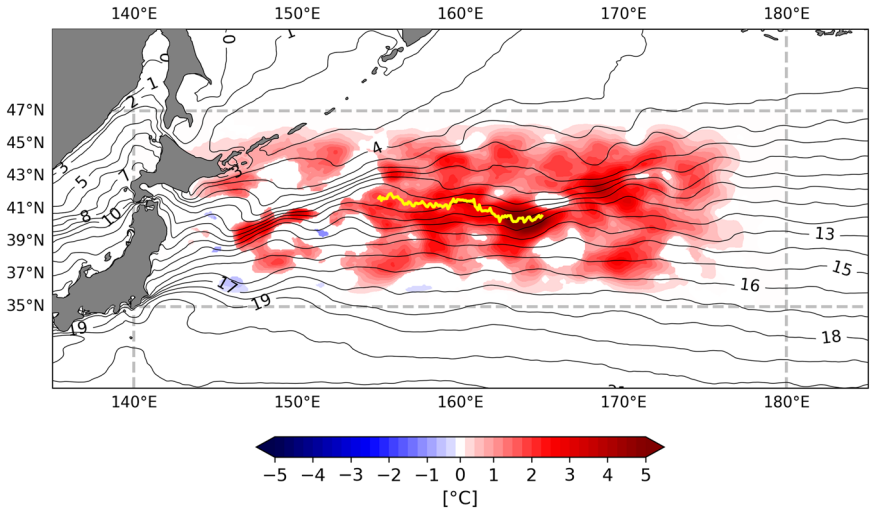

Fig. 2 | SST anomaly forcing structure (color shading; °C), time mean SST frontal location (yellow line), and the SST NDJFM climatology (black contours with contour interval of 3 °C). SST anomaly pattern is obtained by regressing the SST onto the Oyashio Extension Index that represents a northward shift of the SST front, and multiplied by 5. SST anomalies and frontal locations are obtained as described in the "Methods". The dashed lines indicate the domain over which the SST anomaly was applied.

Table 1 | Equations to define the large-scale heating and convective heating, and model variables used in those equations, in VR-CAM6. L_v and C_p stand for the latent heat of vaporization (2.5×10^6 J/kg) and the specific heat at constant pressure (1004 J/kg K), respectively

Variable	Definition / Explanation
Large-scale condensational heating	RCMTEND_CLUBB$*L_v/C_p$ + MPDT/C_p
Convective heating	(STEND_CLUBB – RCMTEND_CLUBB$*L_v$)/C_p + ZMDT + DPDLFT + EVAPTZM
RCMTEND_CLUBB	Cloud Liquid Water Tendency
MPDT	Morrison microphysics heating tendency
STEND_CLUBB	Static energy tendency
ZMDT	Temperature tendency - Zhang-McFarlane moist convection
DPDLFT	Temperature tendency due to deep convective detrainment
EVAPTZM	Temperature tendency - Evaporation/snow production from Zhang convection

localized over the KOE region with a structure that resembles the WBC ocean fronts (Fig. 3a, b). The sum of these two heating terms matches very well with the conventional latent heating output from CAM (DTCOND; temperature tendency due to moist processes) (not shown). Two KOE latent heating components have synoptic temporal variability (Fig. 3c) which will be elaborated on below. The vertical structure of KOE-region-averaged heating climatology shows that convective heating is most pronounced within the atmospheric boundary layer (approximately below 800-hPa) while large-scale heating peaks around 700–800 hPa (Fig. 3d).

We next explore the characteristics of each latent heating type occurring over the KOE region and create an index that identifies days with heating amplitudes that are above normal. First, the KOE-mean latent heating is vertically averaged (weighted by pressure) and its mean seasonal cycle, which is defined as the 3-hourly climatology from CTRL, is removed at each grid point. Since the anomaly is deviation from the climatology of the given time of the day, there is no effect of the diurnal cycle. Then, the 3-hourly timeseries of the spatial mean of the latent heating anomalies within the KOE domain (black box in Fig. 3) is standardized by subtracting its mean and dividing by its standard deviation; this standardized index shall be referred to as the "heating index". The autocorrelations of the two (large-scale condensational and convective) heating indices are shown in Fig. 3c. While both heating indices exhibit synoptic timescales, the large-scale heating index has a shorter e-folding timescale than the convective heating index (1 day *vs.* 2 days; Fig. 3c). As will be explained in Results-b section, this difference in e-folding timescales originates from the two heatings' different enhancement mechanisms and the geographical location of extratropical cyclones in which the heating takes place relative to the KOE region. Figure 3a-c therefore show that the two types of heating have different climatological spatial patterns and timescales, supporting our hypothesis that they are associated with different types of weather systems. Thus, their response to SST forcing may also be distinct from each other.

We define discrete positive heating events as the local maxima of the heating index when the normalized amplitude of the heating index >1 and is separated from neighboring events by at least 5 days. Figure S1 shows an example heating timeseries from one of the ensemble members (1993 November 1st as the initial condition). In this ensemble member, there are 9 (7) large-scale condensational (convective) heating events as noted by star marks. Based on this procedure, we identified 427 (418) positive heating events for the large-scale condensational heating index and 258 (271) positive heating events for the convective heating index in CTRL (WARM) (Table 2). Lead-lag composites of circulation and heating anomalies for each set of positive heating events are computed using the time of peak amplitude within each event as the reference time. The significance level of the composites was tested by Monte Carlo resampling, randomly selecting the same number of random composite samples from the entire heating index time series and repeating this procedure 1000 times. This procedure was applied to large-scale condensational heating and convective heating separately. The first and the last 5 days of the November–January experiment period are not taken into account as 5-day lagged composites will be considered.

Three different types of synoptic weather systems

We first attempt to understand the characteristics of the positive heating events by analyzing the composites from CTRL. Figure 4 shows lagged composites of the large-scale heating and convective heating indices during their respective positive events. When large-scale condensational heating is enhanced over the KOE region, the large-scale heating index peaks at day 0 (by construction) and its growth and decay both occur within about one day, similar to the e-folding timescale of the autocorrelation function (blue line in Fig. 4a). During these events, convective heating (red line in Fig. 4a) peaks about 1 day after the peak of the large-scale heating. The large-scale heating amplitude at day 0 is about 1.7 K/day, which corresponds to about 2.5 normalized amplitude (i.e., the standard deviation of the 3 hourly large-scale heating time series), but the peak amplitude of the associated convective heating at day +1 is only 0.1 K/day, corresponding to a normalized amplitude of 0.4.

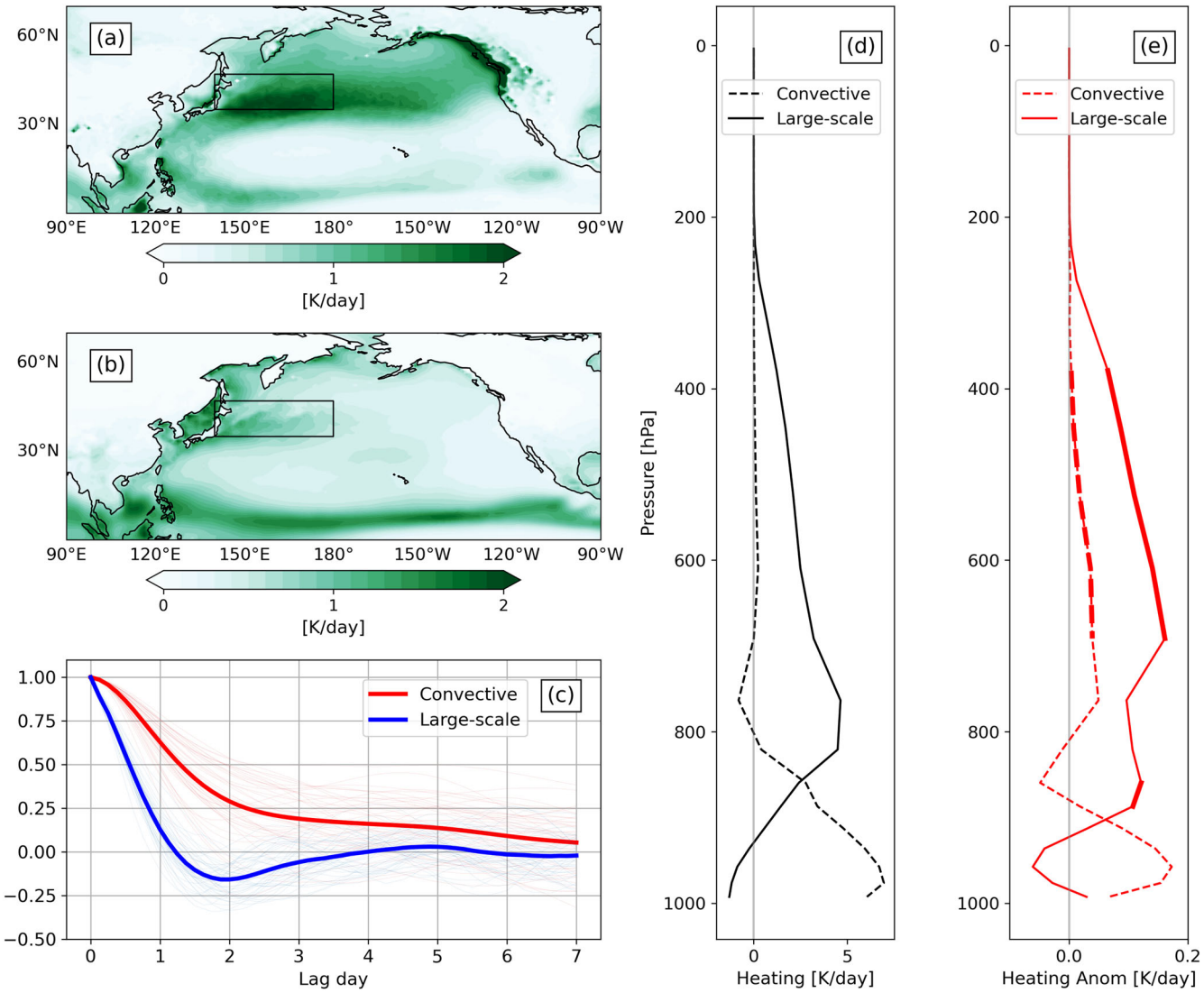

Fig. 3 | Characteristics of two latent heating components. a, **b** Vertically averaged large-scale and convective heating climatology, respectively, of CTRL for November-January (K day^{-1}). Black box represents the KOE region where the SST anomaly forcing is prescribed in WARM. **c** Autocorrelation of large-scale (blue) and convective (red) heatings of CTRL. Thin lines represent the autocorrelation for each ensemble member and the thick line shows the mean of each ensemble's auto-correlations. **d** Vertical structure of KOE-area-mean latent heating (K day^{-1}) from CTRL and (**e**) vertical structure of the latent heating response (WARM minus CTRL) in K day^{-1}. Thick line segments in (**e**) represent statistical significance at 5% level.

Table 2 | Number of large-scale and convective heating events found in CTRL and WARM simulations

CTRL	Large-scale heating events	427 events	232 large-scale heating-only events
	Convective heating events	258 events	132 overlapping events
			65 convective heating-only events
WARM	Large-scale heating events	418 events	219 large-scale heating-only events
	Convective heating events	271 events	129 overlapping events
			74 convective heating-only events

The positive convective heating event composite (Fig. 4b) demonstrates somewhat different characteristics, and its amplitude is generally much smaller than that based on the large-scale heating composite (about 0.5 K/day or close to 2.0 after normalization). While the peak of the convective heating also occurs on day 0 (by construction), the associated large-scale heating index peaks near day^{-1} with an amplitude that is slightly stronger than 0.5 K/day or about 0.8 normalized amplitude (Fig. 4b). The difference between the two composites indicates that the two types of heating may not necessarily be always enhanced within the same weather system. If they were, then their normalized amplitudes would be similar between the two composites. The corresponding composites of surface latent and sensible heat fluxes (green and purple lines in Fig. 4) indicate that convective heating events (Fig. 4b) are associated with strong upward surface turbulent heat fluxes, as

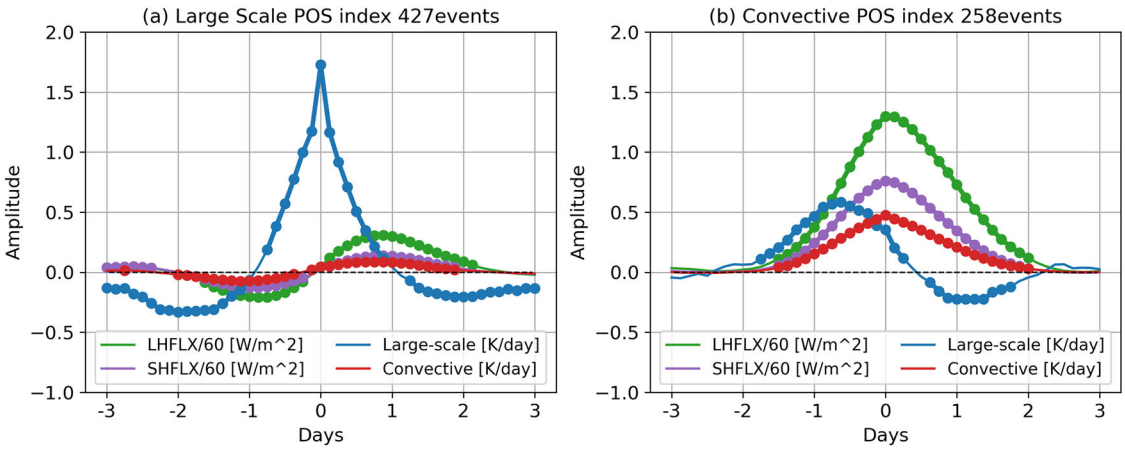

Fig. 4 | Composites of heating indices. Composites during positive (**a**) large-scale and (**b**) convective events from CTRL for KOE-area averaged anomalies of surface latent heat flux (green), surface sensible heat flux (purple), large-scale heating (blue), and convective heating (red) in Wm^{-2}. Latent and sensible heat flux indices are divided by 60 to have similar amplitudes to those of large-scale and convective heating indices. Dotted thick lines indicate statistically significant values at 5% level.

also seen for the convective heating that accompanies large-scale heating events (Fig. 4a).

Both composites suggest a weak 1-day-lagged relationship between the peaks in large-scale and convective heating. Therefore, we further categorize the selected heating events into overlapping and non-overlapping cases. Here, overlapping cases are defined as those convective heating events occurring within a 3-day time period after the occurrence of a large-scale heating event. One such case would reflect the passage of an extratropical cyclone, in which the large-scale heating in the warm sector is followed by shallow convective heating in the cold sector. We find 132 events of this kind. The same 132 cases can also be identified based on selecting the convective heating peak preceded by large-scale heating peak within a 3-day time period. Given that both definitions capture the same dynamical system, we present the large-scale heating peak-centered composites only. In addition to the overlapping cases, we also select large-scale heating-only cases (there are 232 events) for which the large-scale heating peak occurs in the absence of a convective heating peak over a centered 6-day period (e.g., lag −3 to +3 days). Similarly, we also select convective heating-only cases (there are 65) for which the convective heating peak occurs in the absence of a large-scale heating peak over a centered 6-day period. The results remain qualitatively unchanged if we use a centered 4-day period instead of a 6-day period (not shown). Note that there are remaining 62 and 69 events from CTRL and WARM that correspond to cases when large-scale heating follows the convective heating. As these events are not dynamically relevant for the KOE air-sea interaction, we do not consider them in this study.

Figure 5 shows the composite structures associated with these three different categories of cases in CTRL. During the overlapping cases, both large-scale and convective heating anomalies exhibits stronger amplitudes, e.g., the magnitude of the convective heating peak at day +1 (red line in Fig. 5a; ~0.3 K/day) is stronger than the composite amplitude of all combined cases (red line in Fig. 4a; ~0.1 K/day). These overlapping cases are associated with a baroclinic wave structure located over the KOE region (Fig. 5b). The composite map of 850 hPa (contours) and 300 hPa (shading) geopotential height anomalies shows that a low-level cyclonic (anticyclonic) circulation develops over the western (eastern) side of the KOE-box region (Fig. 5b). This low-level circulation is in quadrature with the upper-level wave structure which originates upstream over Eurasia (Fig. S3). Strong amplitudes of large-scale condensational heating during these events are likely to be associated with enhanced moisture advection as anomalous southerly winds on the lee side of the low-level cyclonic circulation would induce an intrusion of warm and moist air originating from the subtropics (Fig. 5c). As the system propagates eastward, cold and dry continental air intrudes into the KOE-region, enhancing convective heating anomalies on the backside of the cyclone at day +1 (Fig. 5d).

During the large-scale heating-only cases, convective heating is muted throughout the duration of the composite large-scale heating event (red line, Fig. 5e). The circulation pattern during these cases is also distinct from that of the overlapping cases. While the low-level and upper-level circulations are still in near-quadrature to form a baroclinic structure, the amplitude of the anticyclonic structure over the central North Pacific is much stronger than that of the overlapping cases, and the weaker cyclonic structure is shifted westward (Fig. 5f). Therefore, following the dipole structure of cyclone and anticyclone, southerly warm moist flow enhances large-scale heating over the entire KOE region (Fig. 5g). However, the weak low-level cyclone located over the western flank of the KOE region dissipates by lag day +1, preventing this system from bringing cold and dry northerly flow that would enhance convective heating (Fig. 5h). It is interesting to note that we found 232 events when large-scale heating events occur without convective heating enhancement, which is much larger than the frequency of occurrence of the other two types of heating events and more than 50% of the total number of events. We infer from this that the dominant weather pattern responsible for latent heating enhancement over the KOE region may not necessarily involve strong low-level cyclones and associated air-sea interaction, in contrast to what has been commonly assumed in previous studies.

The meteorological pattern during the convective heating-only events, which is the rarest among the three categories of events, differs from that of large-scale heating events in that there is a prominent barotropic cyclonic circulation centered over the North Pacific (Fig. 5j). This strong barotropic low pressure system is formed as a cyclonic circulation over the North Pacific and another migratory cyclonic circulation from Siberia merge together over the KOE-region (third column of Fig. S1). The location and the broad extent of this cyclone result in southerly moist flow spread out at day−1 into the central and eastern North Pacific region (Fig. 5k), while the northerly flow induced by the low-level cyclone then causes an intrusion of cold and dry air into the KOE region, enhancing convective heating (Fig. 5l).

These findings indicate that large-scale heating-only and convective heating-only events are associated with distinct meteorological conditions: the former is characterized by an intrusion of southerly warm moist flow within a transient baroclinic system, while the latter is linked to a barotropic cyclonic circulation that advects cold and dry northerly air over the KOE region. These distinctive weather patterns help to explain the different e-folding timescales of the two heating indices (Fig. 3c and Fig. 4). The eastern flank or warm sector of low-level cyclones, where southerly flow and enhanced large-scale condensational heating occurs, tends to evolve and propagate quickly over the KOE region. For example, during the overlapping cases, the composite cyclone takes only about one day to propagate across KOE region such that the southerly flow is located over the central Pacific rather than the KOE region by day +1 (contours in first column of

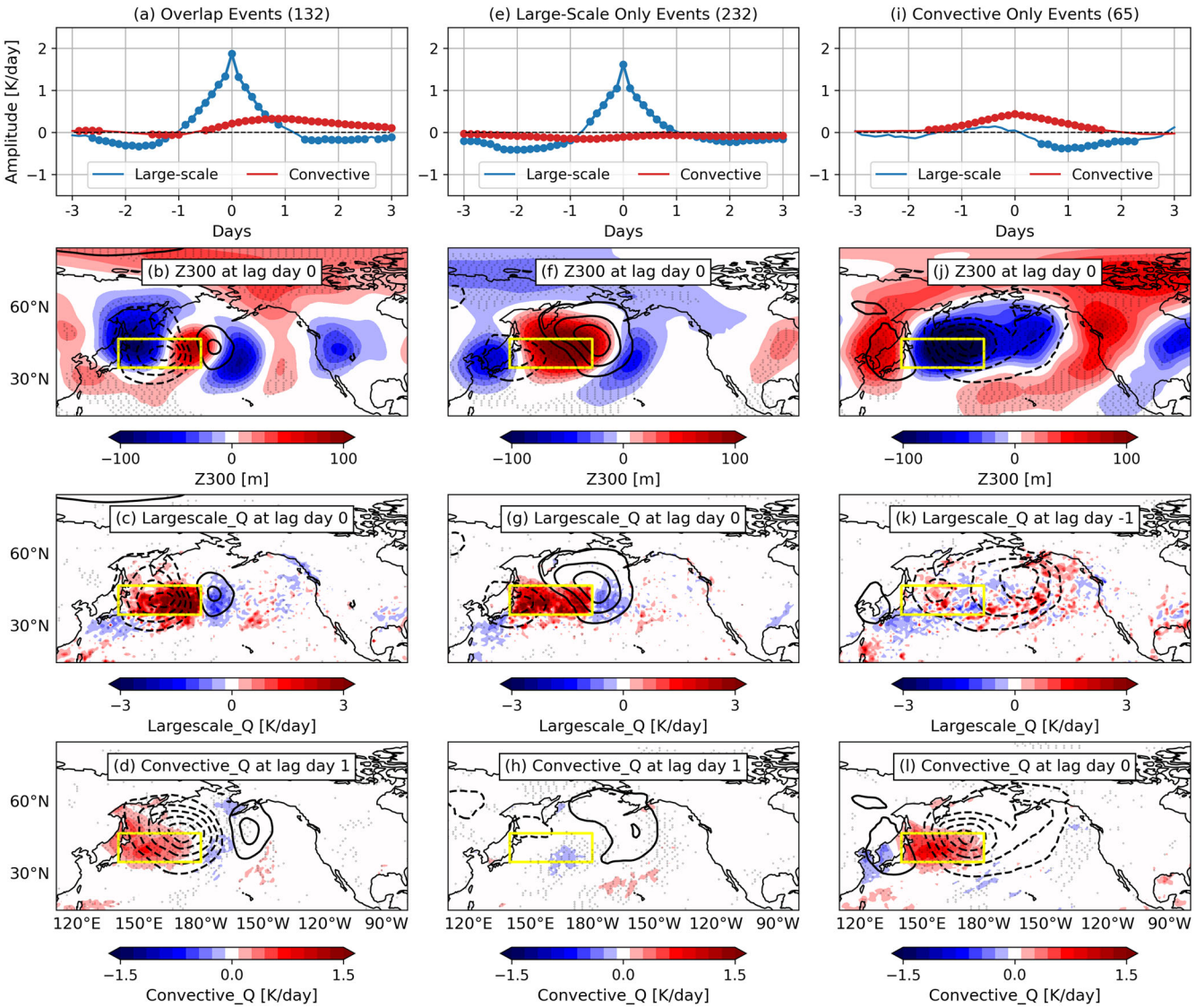

Fig. 5 | Composites for three different types of weather systems based on three different types of heating events from CTRL. Different heating indices (first row), Z300 and Z850 anomaly (shadings and contours of second row, respectively), large-scale heating (third row) and convective heating (fourth row). Three types of events represent (**a**–**d**) overlapping cases when large-scale and convective heating occur together, (**e**–**h**) large-scale heating-only events occurring without convective heating events, and (**i**–**l**) convective heating events-only occurring without large-scale heating events. Numbers in parentheses of the titles of (**a**), (**e**), and (**i**) denote number of events for the corresponding composites. Contours in all the maps show Z850 anomaly composite with contour interval of 20 m. Yellow boxes indicate the KOE region. Note that (**k**) and (**l**) show one lag day earlier than other panels. Dotted thick lines (top row) and dotted grid points (bottom three rows) indicate statistically significant values at 5% level.

Fig. S1). However, as the cyclone matures near the Bering Sea, its propagation speed is reduced, thereby allowing persistent northerly flow to KOE region to provide more favorable conditions for convective heating enhancement (day +1 to +3; first and third column of Fig. S1). Thus, the different circulation structures and their geographical locations relative to the KOE region explain the different timescales of the two latent heating indices.

Our findings on the three distinctive synoptic patterns in the model can be validated by repeating the same procedure but with the JRA55 reanalysis[34]. We chose the JRA55 reanalysis since it provides large-scale condensational heating and convective heating as separate variables. After applying the method described above to 43 NDJ seasons (from Nov 1979/Jan 1980 to Nov 2021/Jan 2022), we have also identified three synoptic weather patterns. Figure S3 shows the composites of the heating indices, circulation, and two heating components during three different synoptic events based on JRA55 reanalysis, which can be directly compared to Fig. 5 based on our model results. The circulation structures of the three synoptic systems are consistent with those identified from the CTRL simulation. As in our model simulation, the baroclinic anticyclonic circulation (second column) is the dominant weather pattern with the most frequent occurrence, although the barotropic cyclonic system (third column) occurs more frequently than baroclinic extratropical cyclone system (first column) in JRA55. The JRA55 reanalysis thus supports that the three synoptic systems and their frequency of occurrence in VR-CAM6 are realistic.

Influence of KOE SST anomalies

Given that the two types of latent heating can be induced by different synoptic conditions, we next examine how warm SST anomalies in the KOE region, indicative of a northward shift of the SST front along the Oyashio Extension, influence the circulation and latent heating structures. Figure 3e shows that the climatology of both heating profiles are enhanced in the WARM simulation. We then repeat our procedures for identifying positive heating events and subdividing them into overlapping and non-overlapping

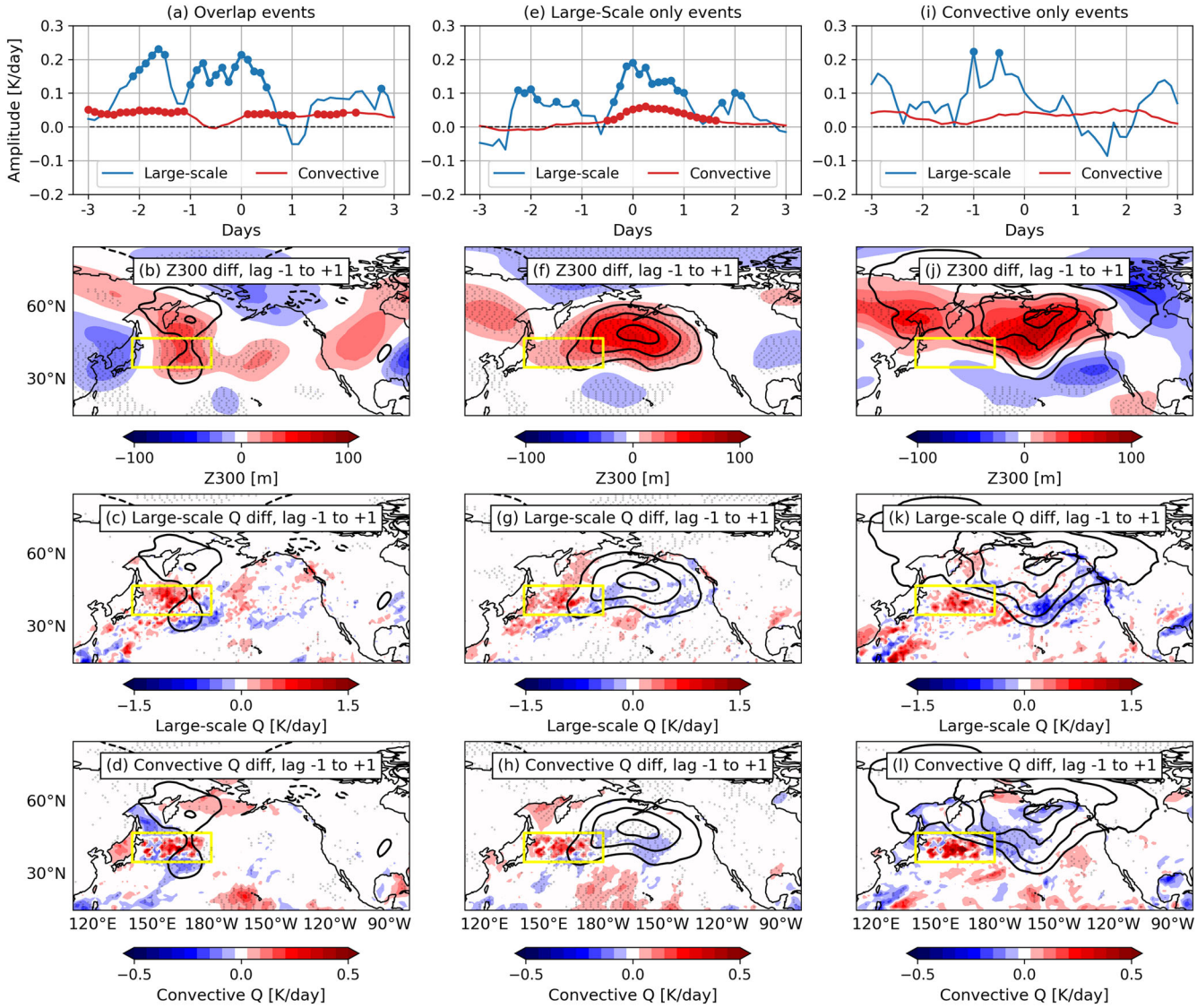

Fig. 6 | As in Fig. 5, but for the composite difference WARM minus CTRL. Different heating indices (first row), Z300 and Z850 anomaly (shadings and contours of second row, respectively), large-scale heating (third row) and convective heating (fourth row). Three types of events represent (**a**–**d**) overlapping cases when large-scale and convective heating occur together, (**e**–**h**) large-scale heating-only events occurring without convective heating events, and (**i**–**l**) convective heating events-only occurring without large-scale heating events. Contours are Z850 (interval of 10 m). To reduce noise, composite difference maps were averaged from lag day -1 to +1. Dotted thick lines (top row) and dotted grid points (bottom 3 rows) indicate statistical significance values at 5% level.

cases to create composites based on WARM. We define anomalies in WARM as deviations from the 3-hourly climatology of CTRL.

Figure 6 shows the responses to the KOE SST anomalies, i.e., the WARM composites for the overlapping and non-overlapping cases minus the corresponding CTRL composites. For the overlapping composite (e.g., when large-scale and convective heating may occur together within a synoptic system), large-scale heating is enhanced by about 10% during the peak of the event (from day −1 to +1; blue line in Fig. 6a) in response to the warmer KOE SST. Prior to the development of the baroclinic system, the convective heating anomaly is about 0.05 K/day, indicating that under the direct influence of the SST anomaly forcing convective heating in WARM is enhanced compared to CTRL (which shows near-zero convective heating anomaly; Fig. 5a vs. 6a). As the system develops from day −1 to day 0, the anticyclonic circulation strengthens slightly (Fig. S4), but subsequently (after day +1) the cyclonic circulation near the KOE region weakens relative to CTRL (first column of Fig. S4). Therefore, the composite difference shows an overall more anticyclonic circulation pattern in WARM (Fig. 6b and third column of Fig. S4). Convective heating is muted between day −1 and day 0 (Fig. 6a and d). The convective heating anomalies are generally positive over the SST forcing region in WARM, resembling the mesoscale SST structure (cf. Fig. 6d and Fig. 2). The large-scale heating is, however, enhanced during this time due to weakened northwesterly flow associated with the anticyclonic response (Fig. 6c).

For the large-scale heating-only event composites, the strong anticyclonic circulation above the KOE region (Fig. 6f and first column of Fig. S5) is substantially enhanced and expanded in WARM (Fig. S5). The WARM anticyclonic circulation response thus shows a barotropic structure centered over the North Pacific (Fig. 6f and third column of Fig. S5). Since the North Pacific anticyclone would bring warm moist air over the KOE region and enhance large-scale condensational heating, the latter is also enhanced by ~10% in WARM (blue line in Fig. 6e, also Fig. 6g). The convective heating also shows an enhancement after about lag day 0 (red line in Fig. 6e). Interestingly, the time evolution of composite difference shows that the anticyclonic response intensifies after day +1 (third column of Fig. S5). This is because in CTRL, the anticyclone starts to dissipate after day +1, but in WARM, it persists until day +3. Given that latent heating plays an important role in inducing a blocking anticyclonic response[35–37], this prolonged circulation may result from the positive feedback between SST

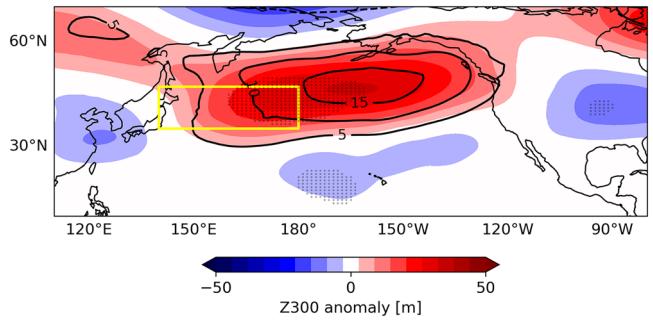

Fig. 7 | The seasonal (NDJ) and ensemble mean response (WARM minus CTRL) pattern of Z300 (m; color shading) and Z850 (contours; interval of 5 m; zero-value contour is omitted). Yellow box indicates the KOE region. Dotted regions indicate statistical significance at 5% level.

anomaly and the anticyclone. In addition to the direct influence of SST on convective heating enhancement after about lag day 0, the anticyclone advects southerly moist air to the KOE-region and together with the SST anomaly-induced updraft, the moist air releases more latent heat to maintain the anticyclone[38–40].

Lastly, for the convective heating-only event composites, the response shows a zonally elongated anticyclonic structure extending from Eurasia to the west coast of North America at upper levels, while the low-level signal is more concentrated over the North Pacific (shadings and contours of Fig. 6j). This represents a weakening and narrowing of the cyclonic circulation in the northeastern part of the KOE region found in CTRL, mainly before the onset of the event (Fig. S6). However, since the composite difference does not resemble the existing wave pattern and the shapes of the upper and lower circulation anomalies do not align with each other as for the large-scale heating-only events, especially after lag day 0, even though they both underwent anticyclonic change, it is difficult to conclude that there is any systematic weakening or strengthening of the original cyclonic circulation pattern (third column of Fig. S6). Similarly, neither latent heating index composite difference shows statistically significant enhancement during WARM compared to CTRL (Fig. 6i, k-l).

It is interesting to note that the composite difference for the large-scale heating-only events resembles the seasonal mean (NDJ) response pattern (Fig. 6f vs. 7). The seasonal mean response in WARM relative to CTRL exhibits a prominent statistically significant barotropic anticyclone centered over the North Pacific, broadly consistent with the high-resolution response from Smirnov et al.[14]. Note that the amplitude of the seasonal mean response is about half of the standard deviation of the CTRL ensemble distribution (not shown). Both the anticyclonic response over the North Pacific and the weak cyclonic responses over the subtropical central North Pacific and eastern half of North America resemble the composite heating event pattern in Fig. 6f. Although the seasonal mean pattern also resembles the convective heating only case (Fig. 6j), given that there are more than 200 large-scale heating-only cases in both CTRL and WARM, which is larger than the sum of the occurrence of the other two cases, the anticyclonic enhancement within this dominant weather pattern may be the primary driver of the mean circulation response to the SST forcing.

Discussion

Using the VR-CAM6 at enhanced resolution over the North Pacific, we have examined the synoptic conditions linked to different types of latent heating over the Kuroshio-Oyashio Extension (KOE) region and the influence of positive SST anomalies on the associated weather systems. First, latent heating was decomposed into two parts: large-scale condensational heating, which is closely associated with resolved processes and moisture flux[32], and convective heating, which represents parametrized convection and latent heating due to boundary layer mixing. The former peaks near the extratropical storm track region, while the latter is preferentially linked to shallow mixing over the KOE oceanic front (and to deep convection over the tropics). Over the KOE region, strong amplitudes of large-scale heating are associated with a baroclinic wave structure and associated southerly warm and moist air intrusions. Depending on the orientation and strength of the low-level anticyclone/cyclone pair, the large-scale condensational heating can be followed by an enhancement of convective heating. On the other hand, strong convective heating without preceding large-scale heating over KOE is linked to a barotropic cyclonic circulation centered over the North Pacific that induces cold and dry continental air intrusions into the KOE region. Because the cyclone extends into the Gulf of Alaska, the large-scale heating spreads into the North Pacific rather than converging over the KOE region. Qualitatively similar synoptic heating systems are identified in the JRA55 reanalysis.

Second, by adding a warm SST anomaly that represents the dominant SST variability over the KOE region, we have shown that these different meteorological patterns respond differently to the imposed SST forcing. While the cyclone-centric baroclinic system did not change appreciably, the anticyclonic baroclinic system is enhanced, likely due to the strengthened updraft and moisture supply from the SST forcing which are important for the maintenance of the anticyclone[35–40]. Smirnov et al.[14] highlighted the importance of resolving small-scale vertical motion to realistically simulate air-sea interactions over the KOE region, but from a seasonal mean point of view. Our analysis further indicates that, in addition to the contribution from parameterized convective heating, large-scale condensational heating within a synoptic weather system, which is closely linked to resolved processes[32], ultimately impacts the seasonal mean circulation response pattern. This study, therefore, shows that quantifying detailed latent heating structures is crucial for a comprehensive understanding of the air-sea coupling mechanism.

Another important conclusion of this study is that the selective enhancement of the most frequently occurring synoptic system, the baroclinic anticyclone, strongly contributes to the seasonal mean response to the SST forcing. Other less frequent types of weather patterns did not respond strongly to the imposed SST anomaly and/or did not occur often enough to influence the seasonal mean response. This finding may help to explain the nonlinear and asymmetric characteristics of the atmospheric response to WBC forcing in general[5,9,10]. While the selective intensification of the synoptic anticyclone under warmer SSTs dominates the seasonal mean response, it remains an open question whether a similar but opposite response would be obtained under a cold SST anomaly associated with a southward shift of the Oyashio Extension and if such a mechanism would scale linearly with the SST anomaly amplitude. It is indeed plausible that other weather patterns, for instance a baroclinic extratropical cyclone or a barotropic Rossby wave-like system, may respond differently to a negative SST anomaly forcing. The combination of each weather pattern's distinctive response could cause the seasonal mean response to be nonlinear and asymmetric as noted in the aforementioned studies[5,9,10]. Furthermore, the characteristics of dominant synoptic patterns may differ in other ocean basins, likely due to relative alignment of the atmospheric jet and the WBC, and different dynamics of the regional intrinsic modes of variability. For example, it would be interesting to explore how various synoptic systems interact with Gulf Stream SST anomalies to impact the North Atlantic and downstream European weather and climate. Thus, in order to advance the understanding of the WBC air-sea interaction mechanism, it would be of much interest to identify the different types of major synoptic weather patterns occurring over that region and study how they react to SST frontal forcing.

In our analysis, we found that the baroclinic system with a prominent upper-level anticyclone but without a strong low-level cyclonic circulation is the dominant weather pattern that strongly enhances latent heating and influences the seasonal mean response to the SST forcing. Conventionally, the influence of SST anomalies on synoptic weather patterns has generally focused on individual extratropical cyclones and weather fronts[22,41,42], although this idea has been questioned by arguing that instead of directly influencing storms, SST anomalies indirectly change the large-scale

environment in which storms develop, thereby playing only a minor role[43–46]. Unlike previous studies that focus on extratropical cyclones, we found that anticyclonic baroclinic systems without an accompanying low-level cyclone contribute most to the seasonal mean circulation response. Our study thus provides a new perspective that the other type of synoptic patterns besides the classical extratropical cyclone structure also induce strong latent heat release over the WBC region, and that their distinctive sensitivities to SST forcing need to be considered to fully understand how oceanic fronts influence climate variability. Our work contributes to recent efforts aimed at distinguishing the role of various synoptic weather patterns over WBC regions[46,47]. In future studies, investigating the factors that determine the dynamical characteristics of various synoptic systems, the degree to which they scale linearly with the SST anomaly amplitude and polarity, as well as how those mechanisms vary in the warm season will help to disentangle the complicated linkages between ocean and atmosphere over the extratropics.

Methods

SST forcing structure

In order to prescribe an SST anomaly that is dominant in the KOE region, we first create an index that captures the latitudinal variability of the SST front along the Oyashio Extension (OE) in the North Pacific. While the SST front is often detected by finding the leading mode of the latitudinal variability of the maximum SST gradient position[6], the central region (155°-165°E) of the KOE domain is associated with strong mesoscale eddy activities and a robust SST pattern associated with SST gradient anomalies can be difficult to be detected[7]. Therefore, we instead use the SST variability itself along the mean position of the front, rather than the latitudinal variability of its gradient, to define the SST forcing structure. This index, referred to as Oyashio Extension Index (OEI), is the normalized principal component (PC) timeseries of the leading mode of the SST variability at temporally fixed mean frontal locations within 155°-165°E as detailed below. They correspond to the largest latitudinal shifts of the OE front, which were shown to occur between 153° and 165°E[6,48].

First, to identify the mean oceanic frontal locations, the value of the meridional SST gradient ($dSST/dy$) for each month is computed using the monthly mean SST from the GLORYS12 reanalysis with 1/12° horizontal resolution[31]. Then, within the region bounded by 35°-47°N and 155°-165°E, the latitudes with the strongest (e.g., most negative) $dSST/dy$ at each longitude are identified. These values indicate the monthly varying positions of the SST front. Finally, for 1993–2020, cold season (November to March; NDJFM) climatology of this SST frontal position is computed[6]. This temporally fixed mean frontal location is shown in Fig. 2 (yellow curve), indicating that the climatological SST frontal position is located at around 40°-42°N.

We then characterize the SST variability along this mean frontal position by performing an empirical orthogonal function (EOF) analysis on the monthly SST anomalies in NDJFM located at the climatological frontal position in the 155°-165°E longitudinal band and define the timeseries of the normalized first PC as the OEI. (Note that individual monthly anomaly values for November-March, thus 5 data points, for each year are used as opposed to the 5-month mean for the EOF calculation) The first EOF pattern explains almost 40% of the total variance and has a large maximum near 164°E, suggesting strong eddy activity (Fig. S7). The SST anomaly regressed onto the normalized PC timeseries represents the dominant SST anomaly variability over the KOE region, and it resembles the SST pattern associated with the northward shift of the OE front (Frankignoul et al. 2011; see their Fig. 5a)[6]. The yearly mean timeseries of this SST-based EOF is correlated with the latitude based EOF PC timeseries with an amplitude of 0.42 (not shown), indicating that the identified pattern is associated with the interannual-to-decadal fluctuation of the SST frontal shift.

We multiply this regression pattern by a factor of 5 to increase the signal-to-noise ratio and consider only those grid points where the regressions are statistically significant at the 10% level according to Student's t test. The SST forcing domain (also referred to as the KOE domain) is 35°-47°N,140°-180°E, excluding small regions that are not part of the North Pacific (140°-142°E and 43°-47°N; Fig. 2). The edges of this domain were smoothed by applying a cosine tapering in both latitudinal and longitudinal directions. Note that the SST amplitude in Fig. 2 is comparable to the marine heat wave events occurred in the KOE region between May and October 2025 when the SST anomalies ranging from about 2–5 °C were observed. Therefore, the forcing magnitude is not unrealistic and may be helpful to diagnose possible circulation response to an unusual extreme event. The anticyclonic mean response to the same SST anomaly structure, but with weaker amplitude corresponding to the 2-standard deviation of the OE index, is broadly similar to Fig. 7, but with substantially weaker magnitude (not shown). Therefore, the response to the varying magnitude of the warm SST anomaly is approximately linear.

As shown in previous studies, SST anomalies over the KOE region can be associated not only with WBC dynamics but also with large-scale modes of variability such as El-Niño Southern Oscillation (ENSO), Pacific Decadal Oscillation (PDO[49]) and North Pacific Gyre Oscillation (NPGO[50]). Therefore, prior to performing the EOF analysis mentioned above, we used multiple linear regression to remove these modes of variability from the SST data used to compute the OEI and define a SST anomaly that is representative of WBC variability. Specifically, the predictors for the multiple regressions are the first three EOFs of SST anomalies in the tropical Pacific (20°S-20°N, 20°E-70°W) to represent ENSO and the first two EOFs of SST anomalies in the North Pacific (20°-70°N, 120°E-120°W) to represent the PDO and NPGO, respectively. We excluded the KOE region (30°-45°N, 130°-180°E) when computing the North Pacific SST EOFs for PDO and NPGO to prevent any contamination by WBC variability[11].

VR-CAM6 and experimental design

As indicated earlier, we use VR-CAM6 within the Community Earth System Model (CESM) version 2.3 framework[26,28,51]. We employ an enhanced horizontal resolution of ~1/8° in the North Pacific while maintaining the rest of the globe in a relatively coarse resolution (~1°) with a narrow transition (~1/4° to ~1/2°) zone between the two resolutions. This mesh grid structure has 261,794 grid points in the horizontal (Fig. 1). VR-CAM6 uses the Cloud Layers Unified by Binormals scheme[52] to parametrize large-scale clouds, shallow convection, and boundary layer mixing. The deep convection, cloud microphysics, and boundary layer drag are represented by Zhang and McFarlane scheme[33], MG2 scheme[53], and Belijaars et al.[54], respectively.

We perform sets of ensemble simulations with each set having 43 members. Each simulation of the ensemble set is initialized from November 1st and integrated for 3 months, thereby focusing on the early winter (November to January; NDJ) when the atmosphere enters the cold season while the ocean temperature remains relatively warm. It is also the season in which the net surface heat flux over the KOE-region is an effective predictor of North Pacific climate[55]. Different initial conditions for each ensemble member are derived from the ERA5 reanalysis' November 1st data of 43 different years from 1979 to 2021[56]. We use zonal and meridional wind (U, V), temperature (T), specific humidity (q), and surface pressure (ps) to create atmospheric initial conditions, using the ERA5 data with 0.25° horizontal resolution and 37 vertical pressure levels. These data are mapped onto the VR-CAM-grid with its 32 vertical levels using the BETACAST software[57,58] to obtain an initial condition with a hydrostatic adjustment to the VR-CAM-grid topography. The prescribed oceanic boundary condition is the monthly climatology of SST and sea-ice concentration from the 1/12° GLORYS12 reanalysis[31] averaged from 1993 to 2020, which is then remapped into CESM-readable 1/10° Parallel Ocean Program (POP) model grid system. In the control (CTRL) simulation, the monthly climatology of SST and sea ice is prescribed. In the perturbation (WARM) experiment, we add a temporally constant SST anomaly forcing pattern described in "Method-A" (Fig. 2). The output data are saved at 3-hourly instantaneous time steps. These outputs are first saved on the VR grid and then remapped onto a nominal 1° grid and 37 pressure levels for the analysis.

Data availability

The ERA5 reanalysis can be accessed in the following webpage: https://cds.climate.copernicus.eu/datasets/reanalysis-era5-single-levels?tab=download, and the GLORYS12 reanalysis data can be accessed in the following webpage: https://data.marine.copernicus.eu/product/GLOBAL_MULTIYEAR_PHY_001_030/description.

Code availability

The CESM2 code is available at https://github.com/ESCOMP/CESM. The BETACAST code to generate initial condition files in variable resolution grid is available at https://github.com/zarzycki/betacast. The analysis code can be requested to the corresponding author with a reasonable request.

Received: 28 October 2025; Accepted: 22 January 2026;
Published online: 03 February 2026

References

1. Nakamura, H., Sampe, T., Tanimoto, Y. & Shimpo, A. Observed associations among storm tracks, jet streams and midlatitude oceanic fronts. *Earth's. Clim. Ocean–Atmos. Interact. Geophys. Monogr.* **147**, 329–345 (2004).
2. Kwon, Y.-O. et al. Role of the Gulf Stream and Kuroshio–Oyashio systems in large-scale atmosphere–ocean interaction: a review. *J. Clim.* **23**, 3249–3281 (2010).
3. Seo, H. et al. Ocean mesoscale and frontal-scale ocean–atmosphere interactions and influence on large-scale climate: a review. *J. Clim.* **36**, 1981–2013, https://doi.org/10.1175/jcli-d-21-0982.1 (2023).
4. Hoskins, B. J. & Karoly, D. J. The steady linear response of a spherical atmosphere to thermal and orographic forcing. *J. Atmos. Sci.* **38**, 1179–1196 (1981).
5. Révelard, A., Frankignoul, C., Sennéchael, N., Kwon, Y.-O. & Qiu, B. Influence of the decadal variability of the Kuroshio Extension on the atmospheric circulation in the cold season. *J. Clim.* **29**, 2123–2144 (2016).
6. Frankignoul, C., Sennéchael, N., Kwon, Y.-O. & Alexander, M. A. Influence of the meridional shifts of the Kuroshio and the Oyashio Extensions on the atmospheric circulation. *J. Clim.* **24**, 762–777 (2011).
7. Hall, R. J. et al. A new robust frontal disturbance index of the Oyashio extension sea surface temperature front. *J. Clim.* **38**, 293–307 (2025).
8. Wills, S. M. & Thompson, D. W. On the observed relationships between wintertime variability in Kuroshio–Oyashio Extension sea surface temperatures and the atmospheric circulation over the North Pacific. *J. Clim.* **31**, 4669–4681 (2018).
9. Kushnir, Y. et al. Atmospheric GCM response to extratropical SST anomalies: synthesis and evaluation. *J. Clim.* **15**, 2233–2256 (2002).
10. Seo, H., Kwon, Y.-O., Joyce, T. M. & Ummenhofer, C. C. On the predominant nonlinear response of the extratropical atmosphere to meridional shifts of the Gulf Stream. *J. Clim.* **30**, 9679–9702, https://doi.org/10.1175/jcli-d-16-0707.1 (2017).
11. Révelard, A., Frankignoul, C. & Kwon, Y.-O. A multivariate estimate of the cold season atmospheric response to North Pacific SST variability. *J. Clim.* **31**, 2771–2796, https://doi.org/10.1175/jcli-d-17-0061.1 (2018).
12. Thomson, S. I. & Vallis, G. K. Atmospheric response to SST anomalies. Part I: background-state dependence, teleconnections, and local effects in winter. *J. Atmos. Sci.* **75**, 4107–4124 (2018).
13. Thomson, S. I. & Vallis, G. K. Atmospheric response to SST anomalies. Part II: background-state dependence, teleconnections, and local effects in summer. *J. Atmos. Sci.* **75**, 4125–4138 (2018).
14. Smirnov, D., Newman, M., Alexander, M. A., Kwon, Y.-O. & Frankignoul, C. Investigating the local atmospheric response to a realistic shift in the Oyashio sea surface temperature front. *J. Clim.* **28**, 1126–1147 (2015).
15. Ma, X. et al. Distant influence of Kuroshio Eddies on North Pacific weather patterns?. *Sci. Rep.* **5**, 17785. https://doi.org/10.1038/srep17785 (2015).
16. Ma, X. et al. Importance of resolving Kuroshio front and eddy influence in simulating the North Pacific Storm Track. *J. Clim.* **30**, 1861–1880, https://doi.org/10.1175/jcli-d-16-0154.1 (2017).
17. Wills, R. C. J., Herrington, A. R., Simpson, I. R. & Battisti, D. S. Resolving weather fronts increases the large-scale circulation response to Gulf Stream SST anomalies in variable-resolution CESM2 simulations. *J. Adv. Model. Earth Syst.* **16**. https://doi.org/10.1029/2023ms004123 (2024).
18. Willison, J., Robinson, W. A. & Lackmann, G. M. The importance of resolving mesoscale latent heating in the North Atlantic storm track. *J. Atmos. Sci.* **70**, 2234–2250 (2013).
19. Willison, J., Robinson, W. A. & Lackmann, G. M. North Atlantic storm-track sensitivity to warming increases with model resolution. *J. Clim.* **28**, 4513–4524 (2015).
20. Wernli, H. & Gray, S. L. The importance of diabatic processes for the dynamics of synoptic-scale extratropical weather systems–a review. *Weather Clim. Dyn.* **5**, 1299–1408 (2024).
21. O'Neill, L. W., Haack, T., Chelton, D. B. & Skyllingstad, E. The Gulf Stream convergence zone in the time-mean winds. *J. Atmos. Sci.* **74**, 2383–2412 (2017).
22. Parfitt, R. & Czaja, A. On the contribution of synoptic transients to the mean atmospheric state in the Gulf Stream region. *Q. J. R. Meteor Soc.* **142**, 1554–1561, https://doi.org/10.1002/qj.2689 (2016).
23. Parfitt, R. & Seo, H. A new framework for near-surface wind convergence over the Kuroshio extension and Gulf Stream in wintertime: the role of atmospheric fronts. *Geophys. Res. Lett.* **45**, 9909–9918 (2018).
24. Siqueira, L. & Kirtman, B. P. Atlantic near-term climate variability and the role of a resolved Gulf Stream. *Geophys. Res. Lett.* **43**, 3964–3972 (2016).
25. Siqueira, L., Kirtman, B. & Laurindo, L. Forecasting remote atmospheric responses to decadal Kuroshio stability transitions. *J. Clim.* **34**, 379–395 (2021).
26. Lauritzen, P. H. et al. NCAR release of CAM-SE in CESM2. 0: a reformulation of the spectral element dynamical core in dry-mass vertical coordinates with comprehensive treatment of condensates and energy. *J. Adv. Model. Earth Syst.* **10**, 1537–1570 (2018).
27. Xu, Z. et al. Evaluating variable-resolution CESM over China and Western United States for use in water-energy nexus and impacts modeling. *J. Geophys. Res. Atmos.* **126**. https://doi.org/10.1029/2020jd034361 (2021).
28. Herrington, A. R. et al. Impact of grids and dynamical cores in CESM2. 2 on the surface mass balance of the Greenland Ice Sheet. *J. Adv. Model. Earth Syst.* **14**, e2022MS003192 (2022).
29. Wijngaard, R. R., Herrington, A. R., Lipscomb, W. H., Leguy, G. R. & An, S.-I. Exploring the ability of the variable-resolution Community Earth System Model to simulate cryospheric–hydrological variables in High Mountain Asia. *Cryosphere* **17**, 3803–3828 (2023).
30. Boza, B., Herrington, A., Ilicak, M., Danabasoglu, G. & Sen, O. L. Exploring climate of the Euro-Mediterranean using a Variable-Resolution Configuration of the Global Community Earth System Model (VR-CESM). *J. Geophys Res.-Atmos.* **130**, e2024JD041300 (2025).
31. Lellouche, J.-M. et al. Recent updates to the Copernicus Marine Service global ocean monitoring and forecasting real-time 1/12° high-resolution system. *Ocean Sci.* **14**, 1093–1126 (2018).
32. Herrington, A. R. & Reed, K. A. On resolution sensitivity in the Community Atmosphere Model. *Q. J. R. Meteor Soc.* **146**, 3789–3807 (2020).
33. Zhang, G. J. & McFarlane, N. A. Sensitivity of climate simulations to the parameterization of cumulus convection in the Canadian Climate Centre general circulation model. *Atmos.-Ocean* **33**, 407–446 (1995).

34. Kobayashi, S. et al. The JRA-55 reanalysis: General specifications and basic characteristics. *J. Meteorol. Soc. Jpn. Ser. II* **93**, 5–48 (2015).
35. Pfahl, S., Schwierz, C., Croci-Maspoli, M., Grams, C. M. & Wernli, H. Importance of latent heat release in ascending air streams for atmospheric blocking. *Nat. Geosci.* **8**, 610–614 (2015).
36. Wenta, M., Grams, C. M., Papritz, L. & Federer, M. Linking Gulf Stream air–sea interactions to the exceptional blocking episode in February 2019: a Lagrangian perspective. *Weather Clim. Dyn.* **5**, 181–209, https://doi.org/10.5194/wcd-5-181-2024 (2024).
37. Steinfeld, D. & Pfahl, S. The role of latent heating in atmospheric blocking dynamics: a global climatology. *Clim. Dyn.* **53**, 6159–6180 (2019).
38. Baggett, C. & Lee, S. Summertime midlatitude weather and climate extremes induced by moisture intrusions to the west of Greenland. *Q. J. R. Meteor Soc.* **145**, 3148–3160 (2019).
39. Kim, D. W. & Lee, S. Relationship between boreal summer circulation trend and destructive stationary–transient wave interference in the western hemisphere. *J. Clim.* **34**, 4989–4999 (2021).
40. Yamamoto, A. et al. Oceanic moisture sources contributing to wintertime Euro-Atlantic blocking. *Weather Clim. Dyn.* **2**, 819–840 (2021).
41. Booth, J. F., Thompson, L., Patoux, J. & Kelly, K. A. Sensitivity of midlatitude storm intensification to perturbations in the sea surface temperature near the Gulf Stream. *Mon. Weather Rev.* **140**, 1241–1256, https://doi.org/10.1175/Mwr-D-11-00195.1 (2012).
42. Parfitt, R., Czaja, A., Minobe, S. & Kuwano-Yoshida, A. The atmospheric frontal response to SST perturbations in the Gulf Stream region. *Geophys. Res. Lett.* **43**, 2299–2306, https://doi.org/10.1002/2016gl067723 (2016).
43. Haualand, K. F. & Spengler, T. Direct and indirect effects of surface fluxes on moist baroclinic development in an idealized framework. *J. Atmos. Sci.* **77**, 3211–3225 (2020).
44. Tsopouridis, L., Spensberger, C. & Spengler, T. Cyclone intensification in the Kuroshio region and its relation to the sea surface temperature front and upper-level forcing. *Q J. R. Meteor Soc.* **147**, 485–500, https://doi.org/10.1002/qj.3929 (2020).
45. Tsopouridis, L., Spengler, T. & Spensberger, C. Smoother versus sharper Gulf Stream and Kuroshio sea surface temperature fronts: effects on cyclones and climatology. *Weather Clim. Dyn.* **2**, 953–970, https://doi.org/10.5194/wcd-2-953-2021 (2021).
46. Reeder, M. J., Spengler, T. & Spensberger, C. The effect of sea surface temperature fronts on atmospheric frontogenesis. *J. Atmos. Sci.* **78**, 1753–1771 (2021).
47. Okajima, S., Nakamura, H. & Spengler, T. Midlatitude oceanic fronts strengthen the hydrological cycle between cyclones and anticyclones. *Geophys. Res. Lett.* **51**, e2023GL106187 (2024).
48. Qiu, B., Chen, S. & Schneider, N. Dynamical links between the decadal variability of the Oyashio and Kuroshio extensions. *J. Clim.* **30**, 9591–9605, https://doi.org/10.1175/jcli-d-17-0397.1 (2017).
49. Mantua, N. J., Hare, S. R., Zhang, Y., Wallace, J. M. & Francis, R. C. A Pacific interdecadal climate oscillation with impacts on salmon production. *Bull. Am. Meteorol. Soc.* **78**, 1069–1080 (1997).
50. Di Lorenzo, E. et al. North Pacific Gyre Oscillation links ocean climate and ecosystem change. *Geophys. Res. Lett.* **35** (2008).
51. Danabasoglu, G. et al. The Community Earth System Model version 2 (CESM2). *J. Adv. Model. Earth Syst.* **12**, e2019MS001916 (2020).
52. Bogenschutz, P. A. et al. Higher-order turbulence closure and its impact on climate simulations in the Community Atmosphere Model. *J. Clim.* **26**, 9655–9676, https://doi.org/10.1175/Jcli-D-13-00075.1 (2013).
53. Gettelman, A. & Morrison, H. Advanced two-moment bulk microphysics for global models. Part I: Off-line tests and comparison with other schemes. *J. Clim.* **28**, 1268–1287 (2015).
54. Beljaars, A. C. M., Brown, A. R. & Wood, N. A new parametrization of turbulent orographic form drag. *Q J. R. Meteor Soc.* **130**, 1327–1347, https://doi.org/10.1256/qj.03.73 (2004).
55. Joh, Y. et al. The role of upper-ocean variations of the Kuroshio-Oyashio Extension in seasonal-to-decadal air-sea heat flux variability. *npj Clim. Atmos. Sci.* **6**, 123 (2023).
56. Hersbach, H. et al. The ERA5 global reanalysis. *Q J. R. Meteor Soc.* **146**, 1999–2049 (2020).
57. Zarzycki, C. M. & Jablonowski, C. Experimental tropical cyclone forecasts using a variable-resolution global model. *Mon. Weather Rev.* **143**, 4012–4037 (2015).
58. Zarzycki, C. zarzycki/betacast: Betacast. (v0.2). https://doi.org/10.5281/zenodo.8184863 (2023).

Acknowledgements

We thank Drs. Arnaud Czaja, Colin Zarzycki, Jongsoo Shin, and Richard Hall for providing useful comments and valuable insights during the course of this work. This research was funded by NSF grants AGS-2040073 and AGS-2055236 through the Climate and Large-scale Dynamics Program. We would like to acknowledge high-performance computing support from the Derecho system (doi:10.5065/qx9a-pg09) provided by the NSF National Center for Atmospheric Research (NCAR), sponsored by the National Science Foundation. The NSF NCAR is a major facility sponsored by the NSF under Cooperative Agreement No. 1852977.

Author contributions

D.W.K. performed model simulations, analyzed the results, and prepared the manuscript draft. Y.O.K., C.F., C.D., and G.D. acquired the funding and supervised the project. A.H. and S.Y.K. helped model experiment set up. All authors interpreted the results and revised the manuscript. All authors have read and approved the manuscript.

Competing interests

The authors declare no competing interests.

Additional information

Supplementary information The online version contains supplementary material available at https://doi.org/10.1038/s41612-026-01340-9.

Correspondence and requests for materials should be addressed to Dong Wan Kim.